Earthquake in a Maze: Compressional Rupture Branching During the 2012 M_W 8.6 Sumatra Earthquake

L. Meng,* J.-P. Ampuero, J. Stock, Z. Duputel, Y. Luo, V. C. Tsai

Seismological observations of the 2012 moment magnitude 8.6 Sumatra earthquake reveal unprecedented complexity of dynamic rupture. The surprisingly large magnitude results from the combination of deep extent, high stress drop, and rupture of multiple faults. Back-projection source imaging indicates that the rupture occurred on distinct planes in an orthogonal conjugate fault system, with relatively slow rupture speed. The east-southeast–west-northwest ruptures add a new dimension to the seismotectonics of the Wharton Basin, which was previously thought to be controlled by north-south strike-slip faulting. The rupture turned twice into the compressive quadrant, against the preferred branching direction predicted by dynamic Coulomb stress calculations. Orthogonal faulting and compressional branching indicate that rupture was controlled by a pressure-insensitive strength of the deep oceanic lithosphere.

The 11 April 2012 moment magnitude (M_w) 8.6 earthquake off shore of Sumatra is a record-breaking event in many respects. It is the largest strike-slip and intraplate earthquake ever recorded and, as shown here, one of the most complicated ruptures ever imaged by modern seismology. The faulting geometry and the peculiarities of its complex rupture path offer a rare opportunity to probe the mechanics of the oceanic lithosphere.

The earthquake occurred in the diffuse deformation zone between the Indian and Australian plates (Fig. 1, left, inset). Its focal mechanism is typical for the region (1), with T axis normal to the Sumatra subduction trench as observed for intraplate oceanic strike-slip earthquakes elsewhere (2) and consistent with regional stress modeling (3). The rupture initiated in the Paleogene oceanic lithosphere formed at the Wharton Basin spreading center but extended unimpeded into the adjacent oceanic lithosphere affected by later volcanism on the Ninetyeast Ridge (NER).

Because of the remote offshore location of this earthquake, geodetic constraints on fault geometry and static slip for teleseismic finite source inversions are unavailable. We imaged the rupture process by means of back-projection of teleseismic data from European and Japanese seismic networks. We applied the Multitaper-MUSIC array processing technique, which provides higher resolution than that of conventional beamforming (4). We also adopted a "reference window" strategy so as to avoid the systematic "swimming" artifact (5). High-frequency (HF, 0.5 to 1 Hz) source radiation is reliably imaged during 160 s (movies S1 and S2). The methods and their resolution and uncertainty analysis are described in the supplementary materials. The spatiotemporal evolution of the main HF sources (Figs. 1 and 2) is remarkably complex. The rupture involved at least three different, almost orthogonal, faults. Their strikes are consistent with the conjugate planes of centroid moment tensor (CMT) solutions and with the distribution of aftershocks (Fig. 1). The rupture process comprises at least three distinct stages (Fig. 1, right, inset), and the rupture length and speed on each fault are shown in Fig. 2. It started as a bilateral rupture on a fault striking WNW-ESE ("fault A") with a rupture length of ~100 km and duration of ~25 s. This stage generated the strongest HF radiation (fig. S3). The rupture then branched into an almost orthogonal fault ("fault B"), breaking bilaterally for ~60 s over 300 km. The onset of rupture to the NNE on fault B was delayed by ~15 s and then propagated until near the Sumatra trench. Fault B's SSW rupture front branched into a third almost orthogonal fault ("fault C"), which ruptured to the NNW for ~100 km. The final rupture stage involved stepping northward from fault C onto a parallel fault ("fault D") that crossed the NER. The total rupture length on faults A, B, and C is 500 km, which is half that obtained by the extrapolation of empirical scaling relations (6). Two hours later, the largest (M_w 8.2) aftershock initiated on the SSE continuation of fault C but ruptured bilaterally for ~100 km on an orthogonal fault (Fig. 1, right).

The magnitude of this earthquake is surprising in an intraplate environment characterized by relatively short faults with wide stepovers. With hindsight, the large magnitude of the 2012 Sumatra earthquake stems from a conjunction of circumstances: wide depth extent, high stress drop, and rupture of multiple faults. Reported centroid depths are below 25 km [U.S. Geological Survey (USGS) CMT/W-phase solution; Global Centroid-Moment-Tensor (GCMT)]. Rupture penetrating into the uppermost mantle is consistent with old and hence thick oceanic lithosphere (~55 million years old, ~35 km) (7). West of the NER, seismic reflection lines show faults cutting through the Moho dis-

continuity (8). Considering uniform slip in a 500-km-long and 40-km-deep rupture, the estimated average slip is ~15 m, and the stress drop is ~15 MPa, which is high but similar to the stress drop of other large oceanic strike-slip earthquakes (9, 10) and not unusual for intraplate and subcrustal earthquakes (11, 12). The multisegment rupture was encouraged by stressing from the M_w 9.1 2004 Sumatra megathrust earthquake, whose southernmost large-slip region coincides with the latitude of the 2012 event (Fig. 1, left). Coulomb stress calculations show that thrust-faulting favors slip on outer-rise strike-slip faults that are oblique to the trench (13).

The dominant E-W rupture of faults A, C, and D adds a new dimension to the prevailing view of the seismotectonics of this region. These faults are subparallel to long-lived but still active faults on the NER (Fig. 3) (14). The bisecting direction of the conjugate faults is consistent with the orientation of the principal stress inferred from seismic and GPS data (15). Strike-slip focal mechanisms from the zone east of the NER have previously been attributed to slip on N-S–striking faults, such as those imaged in seismic lines south of the equator in the Wharton Basin (16). Active E-W–striking faults west of the NER are generally attributed to compressional deformation (8). The rupture geometry of this earthquake indicates that active E-W right-lateral faults are also an important part of the kinematics of this broad deformation zone.

Back-projection imaging reveals rupture on almost orthogonal faults, as confirmed with back-projection of the M_w 8.2 aftershock. This has been observed in earthquake pairs (such as 1987 M_w 6.2 Superstition Hills and M_w 6.7 Elmore Ranch; and 1992 M_w 7.3 Landers and M_w 6.5 Big Bear) but only rarely during single events, such as in the 13 May 1997 M_w 6 Kagoshima earthquake (17) and in the 2000 M_w 7.8 Wharton Basin earthquake (9), although orthogonal faulting of the latter is not confirmed by later studies (18). A multiple CMT inversion (methods are available in the supplementary materials) yields two subevents with similar mechanisms; the second one was ~200 km SW of the hypocenter (Fig. 1, left), which is consistent with rupture on the SSW branch of fault B and on fault C. In the crust, conjugate shear faults intersect at an angle of ~60°. The seafloor magnetic patterns (Fig. 1, right) rule out reactivation of fossil systems of transform faults and ridges. The wide angle between these faults requires pressure-insensitive strength during their formation (Fig. 2, inset).

The rupture path of this earthquake is unexpected: In two occasions, the rupture branched preferably into the compressive (strengthened) quadrant, with arrest or delay in the alternative branch. The NNW-ward rupture front on the right-lateral fault A first turned left into the SSW segment of fault B. Rupture on the NNE segment of fault B was delayed by ~15 s. This behavior is mirrored by the second branching episode. The SSW-ward rupture front on the

Seismological Laboratory, Division of Geological and Planetary Sciences, California Institute of Technology, Pasadena, CA 91125, USA.

*To whom correspondence should be addressed. E-mail: lsmeng@gps.caltech.edu

left-lateral fault B turned right into the NNW segment of fault C. In both cases, the preferred branching direction is toward the compressive quadrant of the previous segment, which is opposite to the expectation based on usual values of friction coefficient. Analysis of the dynamic stresses induced near the tip of a right-lateral crack on orthogonal left-lateral faults (Fig. 2, right) shows that the observed branching direction requires two circumstances: low rupture speed ($\frac{V_r}{V_s} \sim 0.5$, where V_r is the rupture speed and V_s is the shear-wave speed) and low apparent friction coefficient (~0.2)—a small slope of the failure envelope in a shear-versus-normal stress diagram (Fig. 2, inset). The former is robustly supported by our back-projection results: The overall rupture speed is ~2.5 km/s on faults A and B (Fig. 2, left), which is not unusual compared with global average values but is slow compared with wave speeds below the oceanic Moho (50 to 60% of S wave speed) (19). The latter implies a pressure-insensitive strength, which is characteristic of ductile materials at depth. An alternative explanation by poroelastic effects (20)

with large Skempton's coefficient requires high fluid pressure that is inconsistent with the large stress drop.

Sustained seismic rupture also requires a dynamic weakening mechanism. The relatively slow rupture speed suggests scale-dependent energy dissipation by the rupture process. The ductile shear heating instability proposed by (21, 22) operates between 600 and 800°C, which is limited to a roughly 40 to 60 km depth. Serpentinized peridotite has low pressure sensitivity at confining pressures over few 100 MPa, with apparent friction coefficients as low as 0.15 (23), and might dynamically weaken by dehydration embrittlement (24). However, the serpentinization reaction is possible only up to 400 to 500°C, which corresponds to ~25 km depth (8). A single dynamic weakening mechanism that can operate over the whole depth range of slip of this earthquake remains to be identified.

This is not the first time an earthquake has grown larger than expected or has occurred where it is least expected. The destructive 2011 M_w 9.0 Tohoku-Oki and M_w 6.3 Christchurch earthquakes

illustrate the scientific challenge of estimating the likelihood of extreme events based on a short and incomplete historical record. The 2012 Sumatra earthquake raises the concern of similarly large events in continental strike-slip fault systems, which pose a higher hazard to populations. Although the tectonic setting in an oceanic intraplate zone of high deformation is rare, at least one of the ingredients that made this earthquake big—its large stress drop—is a general feature of other intraplate earthquakes (11). Its rupture complexity highlights the importance of considering earthquake scenarios with multisegment ruptures. The rupture transition from faults C and D across an offset larger than 20 km is particularly extreme (25). The relation to the 2004 Sumatra earthquake suggests that large outer-rise events induced by megathrust events—although not producing damaging shaking because of their remote off-shore location—can pose a tsunami hazard if they have a dip component (26) or displace high topography (27). The Gorda plate in the southern Cascadia subduction zone is such an example.
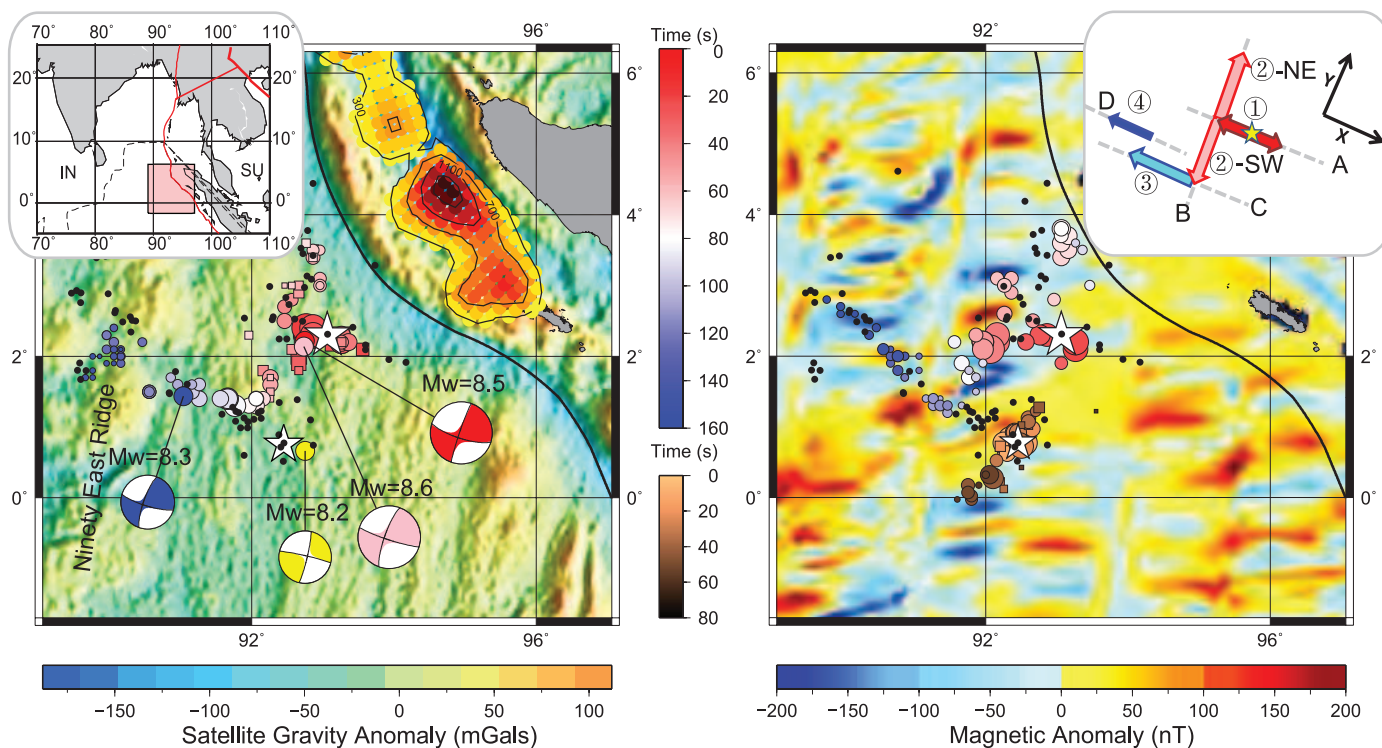

Fig. 1. Spatiotemporal distribution of HF radiation imaged by the (**left**) European and (**right**) Japanese networks. Colored circles and squares indicate the positions of primary and secondary peak HF radiation (from movies S1 and S2, respectively). Their size is scaled by beamforming amplitude, and their color indicates timing relative to hypocentral time (color scale in center). The secondary peaks of the MUSIC pseudo-spectrum are those at least 50% as large as the main peak in the same frame. The brown shaded circles in the right figure are the HF radiation peaks from the M_w 8.2 aftershock observed from Japan. The colored contours in the Sumatra subduction zone (left) represent the slip model of the 2004 M_w 9.1 Sumatra earthquake (28). The figure background is colored by the satellite gravity anomaly (left) in milligalileos (mgals) (color scale on bottom left) and the magnetic anomaly (right) in nanoteslas (color scale on bottom right). Black dots are the epicenters of the first day of aftershocks from the U.S. National Earthquake Information Center catalog. The big and small white stars indicate the hypocenter of the mainshock and M_w 8.2 aftershock. The moment tensors of the M_w 8.6 mainshock, M_w 8.2 aftershock, and double CMT solutions of the mainshock are shown as colored pink, yellow, red, and blue beach balls. The red line in the top left inset shows the boundary between the India (IN) and Sundaland (SU) plates (29). The patterned pink area is the diffuse deformation zone between the India and Australia plate. The red rectangular zone indicates the study area. The top right inset shows the interpreted fault planes (gray dashed lines) and rupture directions (colored arrows).
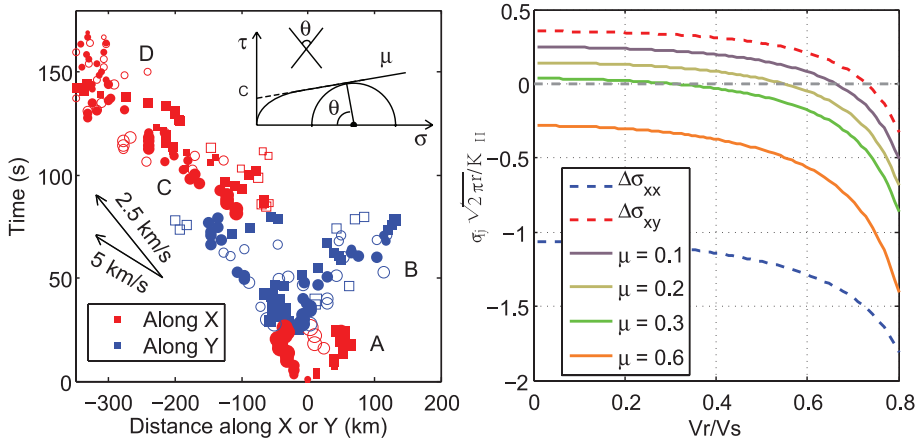
Fig. 2. Spatiotemporal details of the rupture process. (**Left**) Timing and position of the HF radiators relative to the hypocenter. The position is reported in alternation along the axes labeled X (red) and Y (blue) in Fig. 1, inset. Circles and squares are the results of Europe and Japan arrays, respectively. Solid and open symbols indicate principal and secondary HF radiators, respectively. (Inset) Shear strength (τ) versus normal stress (σ) diagram of a nonlinear strength envelope with small apparent friction coefficient μ (almost pressure-insensitive material) and large cohesion C, resulting in almost orthogonal failure planes ($\theta \sim 90°$). (**Right**) Dynamic Coulomb stress changes induced near the tip of a right-lateral crack propagating at steady rupture speed, resolved onto orthogonal left-lateral faults in the compressional quadrant as a function of the ratio between rupture speed and shear-wave speed (V_r/V_s) (30). The symbols denote dynamic changes of normal stress ($\Delta\sigma_{xx}$, negative compressive, blue dashed line), shear stress ($\Delta\sigma_{xy}$, positive left-lateral, red dashed line), and Coulomb stress ($\Delta\sigma_{xy} + \mu\Delta\sigma_{xx}$, color solid curves, assuming various apparent friction coefficients μ indicated in the legend). Stresses are normalized based on the Mode II stress intensity factor (K_{II}) and the distance to the crack tip (r). Rupture on the compressive side can be triggered (positive Coulomb stress change) only for low enough apparent friction and rupture speed.

Fig. 3. Bathymetry where the rupture crosses the NER. Colored background is global bathymetry from SRTM30+ overlain by multibeam bathymetry from cruise KNOX06RR and cruise DYNAMO, respectively. Black dots indicate aftershocks, and circles indicate HF source radiators. These indicate rupture through the NER during the last 15 s of the earthquake. The rupture plane is consistent with numerous fault scarps visible in the multibeam bathymetry.
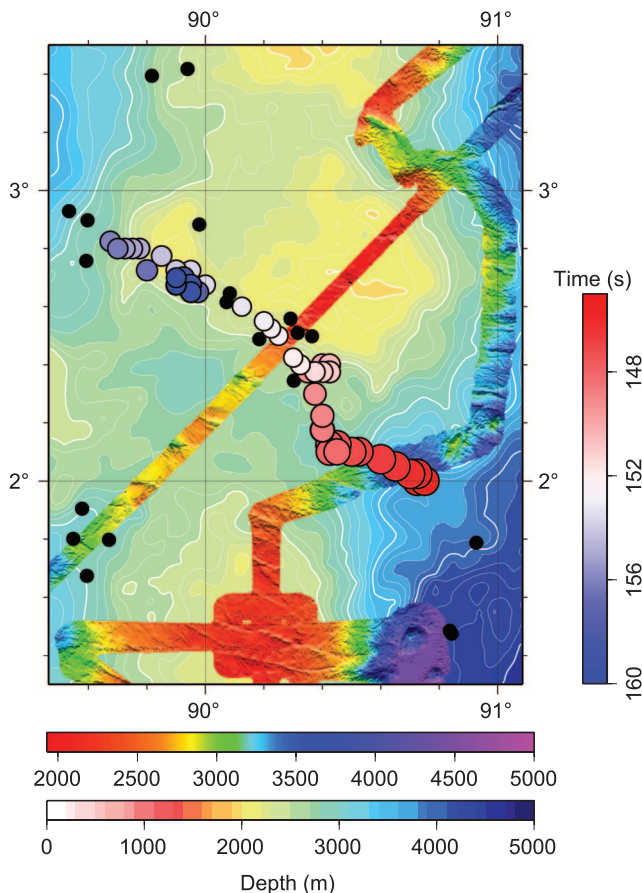
References and Notes

1. E. R. Engdahl, A. Villasenor, H. R. DeShon, C. H. Thurber, *Bull. Seismol. Soc. Am.* **97**, S43 (2007).
2. G. L. Choy, A. McGarr, *Geophys. J. Int.* **150**, 506 (2002).
3. S. Cloetingh, R. Wortel, *Tectonophysics* **132**, 49 (1986).
4. L. Meng, A. Inbal, J. P. Ampuero, *Geophys. Res. Lett.* **38**, L00G07 (2011).
5. L. Meng, J. P. Ampuero, Y. Luo, W. Wu, S. Ni, *Earth Planets Space* 10.5047/eps.2012.05.010 (2012).
6. D. L. Wells, K. J. Coppersmith, *Bull. Seismol. Soc. Am.* **84**, 974 (1994).
7. D. A. Wiens, S. Stein, *J. Geophys. Res.* **88**, 6455 (1983).
8. M. Delescluse, N. Chamot-Rooke, *Earth Planet. Sci. Lett.* **276**, 140 (2008).
9. D. P. Robinson, C. Henry, S. Das, J. H. Woodhouse, *Science* **292**, 1145 (2001).
10. M. Antolik, A. Kaverina, D. S. Dreger, *J. Geophys. Res. Solid Earth* **105**, 23825 (2000).
11. B. P. Allmann, P. M. Shearer, *J. Geophys. Res.* **114**, B01310 (2009).
12. A. Oth, D. Bindi, S. Parolai, D. Di Giacomo, *Geophys. Res. Lett.* **37**, L19304 (2010).
13. J. C. Rollins, R. S. Stein, *J. Geophys. Res.* **115**, B12306 (2010).
14. W. W. Sager *et al.*, *Geophys. Res. Lett.* **37**, L17304 (2010).
15. M. Delescluse, N. Chamotrooke, *Geophys. J. Int.* **168**, 818 (2007).
16. C. Deplus *et al.*, *Geology* **26**, 131 (1998).
17. H. Horikawa, *Bull. Seismol. Soc. Am.* **91**, 112 (2001).
18. R. E. Abercrombie, M. Antolik, G. Ekstrom, *J. Geophys. Res.* **108**, (B1), 2018 (2003).
19. F. Klingelhoefer *et al.*, *J. Geophys. Res.* **115**, B01304 (2010).
20. M. Cocco, J. R. Rice, *J. Geophys. Res.* **107**, 2030 (2002).
21. P. B. Kelemen, G. Hirth, *Nature* **446**, 787 (2007).
22. J. J. McGuire, G. C. Beroza, *Science* **336**, 1118 (2012).
23. J. Escartín, G. Hirth, B. Evans, *Geology* **29**, 1023 (2001).
24. H. Jung, H. W. Green II, L. F. Dobrzhinetskaya, *Nature* **428**, 545 (2004).
25. S. G. Wesnousky, *Nature* **444**, 358 (2006).
26. T. Lay, C. J. Ammon, H. Kanamori, M. J. Kim, L. Xue, *Earth Planets Space* **63**, 713 (2011).
27. Y. Tanioka, K. Satake, *Geophys. Res. Lett.* **23**, 861 (1996).
28. M. Chlieh *et al.*, *Bull. Seismol. Soc. Am.* **97**, S152 (2007).
29. C. DeMets, R. G. Gordon, D. F. Argus, *Geophys. J. Int.* **181**, 1 (2010).
30. A. N. B. Poliakov, R. Dmowska, J. R. Rice, *J. Geophys. Res.* **107**, 2295 (2002).

Supplementary Materials